IEEE Sensors Council

A 24-GHz Frequency-Locked Loop-Based Microwave Microfluidic Sensor for Concentration Detection

Hsiu-Che Chang ⓘ, Chung-Tse Michael Wu ⓘ, *Senior Member, IEEE*, and Chao-Hsiung Tseng ⓘ, *Senior Member, IEEE*

Abstract—**This article presents a 24-GHz microfluidic sensor using frequency-locked loop (FLL) technology for detecting liquid concentrations. The sensor, based on FLL, features a microfluidic channel placed over an asymmetrical coplanar waveguide resonator (ACPWR) that functions as a sensing device. For testing purposes, we use ethanol–water mixtures and glucose–water solutions as the liquid under test. Due to the electric field distribution in media with varying dielectric constants, the phase of the signal undergoes different phase deviations. The FLL-based sensor is capable of detecting these phase deviations and, in response, produces a frequency-modulated signal. This signal is subsequently demodulated into a corresponding voltage with the aid of a frequency demodulator, realized through a phase detector. Consequently, the sensor demonstrates the capability to differentiate between tested liquids of varying concentrations and offers a linear response that correlates the output voltage with the liquid concentration. The proposed 24-GHz FLL microfluidic sensor offers advantages, such as cost effective, high sensitivity, and compact size. It has a great possibility to implement this sensor using the system-on-chip technology. As it combined with Internet of Things technologies, it may have a capability of real-time biomedical specimen sensing for daily life.**

Index Terms—**Asymmetrical coplanar waveguide resonator (ACPWR), frequency-locked loop (FLL), liquid concentration measurement, liquid concentration sensor, microwave microfluidic sensor.**

I. INTRODUCTION

MICROFLUIDIC chips typically employ channels with dimensions ranging from tens to hundreds of micrometers (μm) to manipulate fluid volumes from microliter (μL) to picoliter (pL). This technology boasts efficient sample processing, requiring minimal sample and reagent volumes. The benefits, such as enhanced system stability, reduced energy consumption, decreased required liquid-under-test (LUT) volume, and savings in time and labor, have bolstered the application of microfluidics in point-of-care diagnostics [1], [2]. Its applications span across clinical chemistry [3], cell counting and sorting [4], and nucleic acid detection [5], offering significant advantages. Conventionally, microfluidic chips analyses have relied on the differential light refraction or transmission properties of the LUT [6], [7]. However, this optical method has its limitations. For instance, microfluidic chips must be fabricated from transparent materials and require a complementary optical detection system. Moreover, it solely detects variations in light intensity.

Electromagnetic (EM) waves, in contrast, can discern not only signal intensity but also phase deviation. This adds an extra dimension, enhancing the precision in determining the characteristics of the LUT. Recent studies have explored the potential of EM waves in microfluidic detection. Most of these sensing systems leverage passive components. Nonetheless, they come with their own set of challenges, such as the need for equipment that can generate and read signals, such as network analyzers. To this end, an emerging research direction is to maintain measurement accuracy while seeking alternatives to cumbersome network analyzers, aiming for the portability of the entire sensing system. Furthermore, by integrating Internet of Things (IoT) technology, remote and precise physiological signal measurements could be realized through handheld electronic devices, paving the way for personalized telemedicine.

In the context of EM wave-based sensors, numerous studies have delved into various microfluidic measurements, broadly categorizing sensors into passive and active types. Passive sensors rely on external instruments, such as network analyzers, to generate signals. These signals are then detected through different sensing components, such as the branch line coupler [8], step-impedance microstrip line terminated with a slot resonator [9], *LC* resonator [10], split-ring resonator (SRR) [11], [12], complementary split-ring resonator (CSRR) [13], substrate-integrated waveguide (SIW) resonator [14], [15], and interdigitated capacitive filter sensor [16]. However, the quest for portable electronic device measurements necessitates an alternative to the cumbersome network analyzer.

Hsiu-Che Chang and Chung-Tse Michael Wu are with the Department of Electrical Engineering, National Taiwan University, Taipei 10617, Taiwan (e-mail: ctmwu@ntu.edu.tw).

Chao-Hsiung Tseng is with the Institute of Space System Engineering, National Yang Ming Chiao Tung University, Hsinchu 300, Taiwan (e-mail: chtseng@ieee.org).
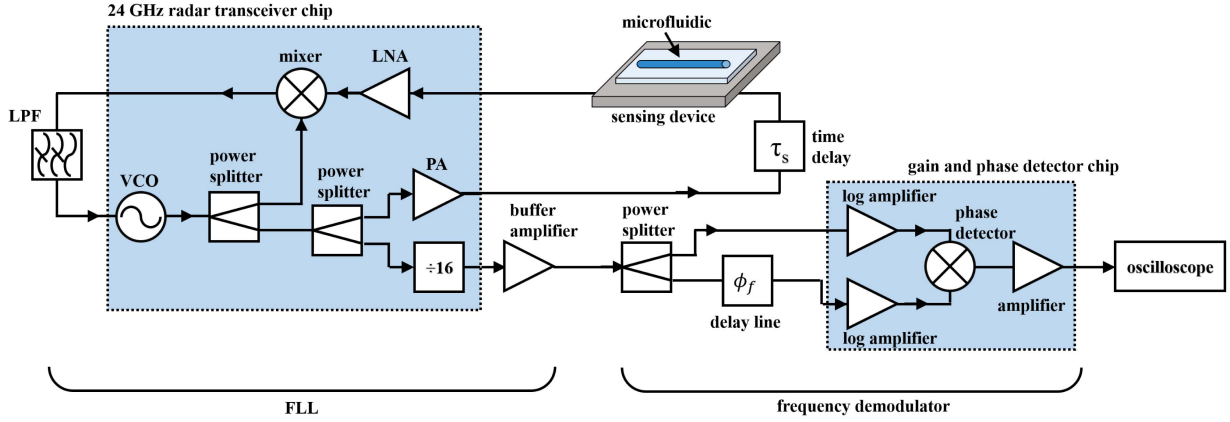
Fig. 1. System block diagram of the proposed FLL-based microfluidic concentration sensor.

On the other hand, active sensors generate their own signal source. They incorporate components, such as voltage-controlled oscillators (VCO), and are often integrated with passive sensing elements, resulting in a robust active sensing system. These systems exhibit a rich variety, including phase-locked loop (PLL) sensor [17], [18], [19], oscillator-based sensor [20], [21], [22], interdigital capacitive sensors [23], and frequency-locked loop (FLL)-based sensors [24].

Compared with other oscillator-based sensing technologies [20], [22], FLL-based sensors exhibit superior frequency stability and precision. Furthermore, FLL-based sensors are characterized by their expansive dynamic range, making them exceptionally suitable for diverse applications, especially where the properties of the analyzed substance vary significantly. In addition, the versatility of the sensing device in FLL-based systems is noteworthy; it can be adapted to various microfluidic channels, thereby enhancing its applicability in a range of sensing measurements. Leveraging these advantages, the system block diagram of the proposed FLL-based microfluidic concentration sensor is shown in Fig. 1, comprising a VCO, mixer, sensing device, loop filter [which in this study is essentially a low-pass filter (LPF)] and a frequency demodulator.

To illustrate, the electric field causes a corresponding phase delay in the signal due to the varying dielectric constants (ϵ_r) of the propagation media. After amplification, the signal enters the RF port of the mixer. Here, the mixer functions as a phase detector, receiving the reference signal from the VCO at its local oscillator (LO) port for phase demodulation. The mixer, depending on the phase deviation it demodulates, outputs a corresponding dc current. This current, after undergoing high-frequency harmonic filtration by the LPF, is converted into a dc voltage and then fed back to the VCO. This feedback alters the VCO's output frequency, thus establishing an FLL. Once the FLL reaches a locked state, the output signal is divided by 16 using a frequency divider before being outputted. The system converts the phase deviation into a corresponding dc voltage, outputting it as the modulated frequency, which can be observed using a spectrum analyzer. For added convenience, a frequency demodulator is incorporated after the FLL-based sensor. The signal is split into two paths before the demodulator; one path feeds directly as a reference signal, while the other passes through a delay line before entering the demodulator. The delay line, depending on the input frequency, produces varying phase shifts for different frequencies. The phase detector then compares the phases of the two signals and outputs a corresponding voltage.

The rest of this article is organized as follows. Section II will explain the principles and design process of the FLL-based sensor. Subsequently, it will be validated using an ethanol–water mixture. Section III will discuss the principles and implementation of the frequency demodulator. In Section IV, the FLL-based system and frequency demodulator will be combined, using both ethanol–water mixtures and glucose–water solutions as LUTs for measurements. Finally, Section V concludes this article.

II. DESIGN OF THE FLL-BASED SENSOR

The FLL-based sensor comprises both the sensing device and the FLL. The sensing device is made up of the sensing element and the microfluidic channel. Conversely, the FLL consists of components, such as the VCO, mixer, and LPF. In the subsequent sections, we will discuss the design process and principles of both the sensing device and the FLL separately.

A. Sensing Device

First, through the following mathematical expression, the relationship between the phase and ϵ_r can be discerned:

$$\Delta\phi = \frac{\omega \cdot \sqrt{\epsilon_r} \cdot \Delta d}{c}. \tag{1}$$

It can be observed from (1) that the phase shift of the signal passing through a medium is directly proportional to the dielectric constant of that medium. The sensing device consists of the sensing element and the microfluidic channel. To accommodate the shape of the microfluidic channel, the asymmetrical coplanar waveguide resonator (ACPWR) is used as the sensing element. The microfluidic channel was placed on the gap between the signal line and the coplanar ground, maximizing its influence on the electric field. The electric field distribution cross-sectional diagram of ACPWR is shown in the Fig. 2.
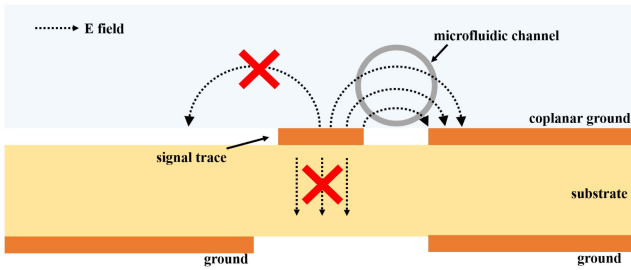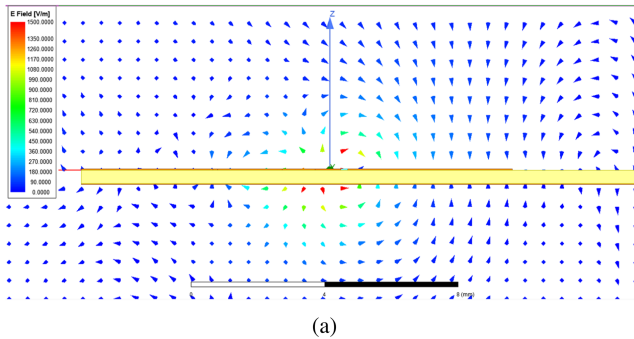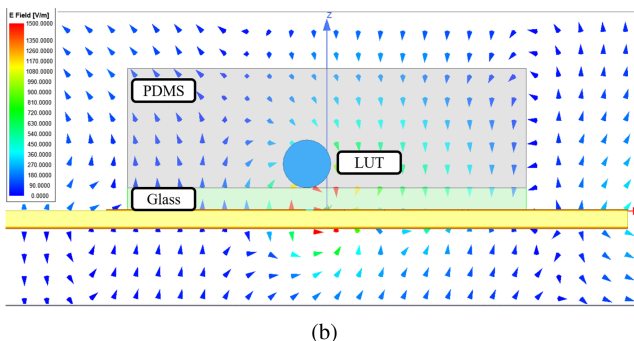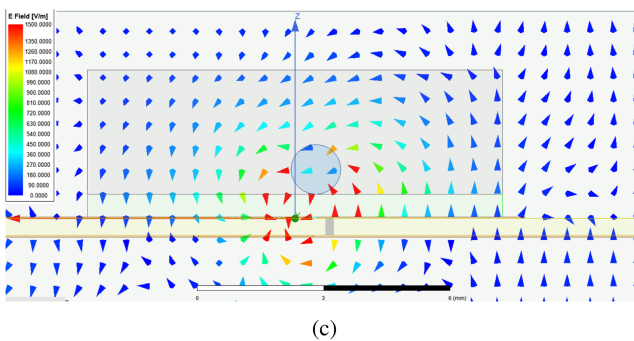
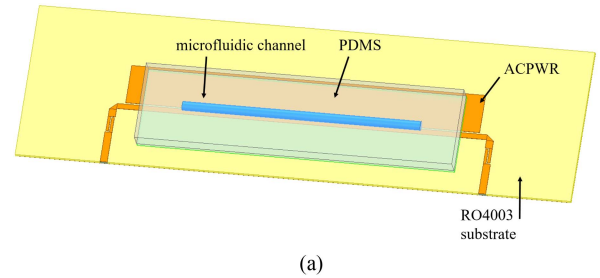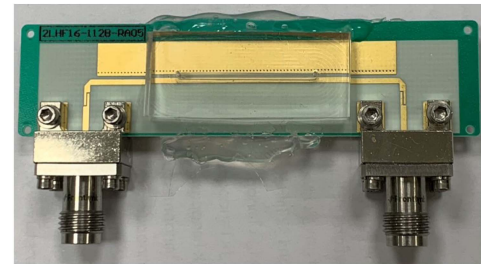Fig. 2.   Electric field distribution cross-sectional diagram of ACPWR.

Fig. 3.   Electric field distributions. (a) Without microfluidic channel. (b) With EVF 0%. (c) With EVF 100%.

Fig. 4.   (a) Schematic 3-D view and (b) implementation of sensing device.

electric field distribution for ACPWR, and LUT concentration at EVF 0%, as well as ACWPR with LUT concentration at EVF 100%, verify the efficacy of the structure.

The schematic 3-D view of the sensing device is shown in Fig. 4(a) and the implemented sensing device is depicted in Fig. 4(b).

The structure of the ACPWR is based on the foundation of conductor-backed coplanar waveguide. In order to concentrate the electric field distribution on the gap where microfluidic channel is placed, the ground beneath the signal line is hollowed out, constraining the electric field to flow only toward the upper coplanar ground. Further, by hollowing out one side of the upper coplanar ground, the electric field becomes even more concentrated between the signal line and the remaining side of the coplanar ground, resulting in an asymmetric coplanar waveguide. In addition, by extending the feed microstrip line and bending it 90°, and feeding it using a coupled line approach, it transforms into a resonator. We refer to it as ACPWR. ACPWR not only enhances the electric field density but also focuses it to traverse through the microfluidic channel before propagating to the other side of the ground, amplifying the phase influence of the LUT.

The microfluidic channel is made of polydimethylsiloxane (PDMS) material and is formed as a long channel on a glass slide. The thickness of the PDMS and the glass slide is 3 and 0.55 mm, respectively. The channel in PDMS can approximately hold up to 20 μL of liquid. The ACPWR is designed at the frequency of 24 GHz using an Ansys HFSS and is fabricated on a Rogers RO4003 C substrate with a thickness of 0.508 mm, a dielectric constant of 3.55, and a loss tangent of 0.0027. Using mixtures with ethanol volume fractions (EVFs) ranging from 0% to 100% as the LUT, they are individually injected into the microfluidic channel to observe the phase deviation of ACPWR's S_{21}. The simulated S_{21} as shown in Fig. 5. According to the results in

To verify if the electric field concentrates at the location where the LUT is positioned as anticipated, we conduct a simulation of the ACPWR and the cross-sectional electric field distribution in the microfluidic channel using high-frequency structure simulator (HFSS), as shown in Fig. 3. As can be seen, the observed
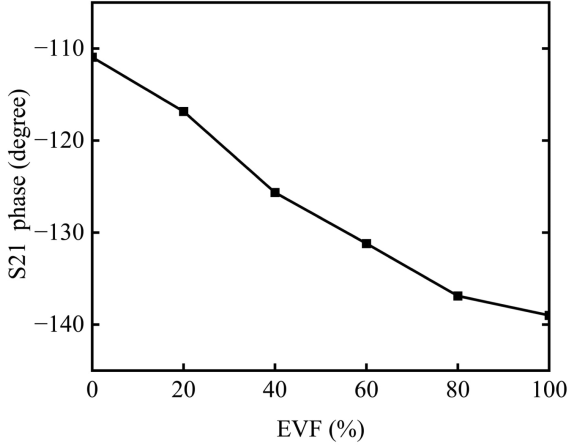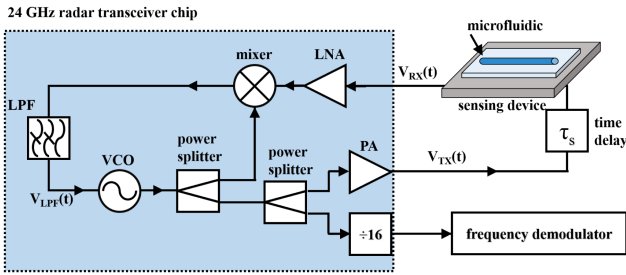
Fig. 5. Simulated ACPWR S_{21} phase deviation.

Fig. 6. System block diagram of FLL.

Fig. 5, ACPWR can distinguish different concentrations of LUT, indicating variations in ε_r.

B. Frequency-Locked Loop

Fig. 6 presents the system block diagram of the FLL, which includes the VCO, mixer, and loop filter. This study utilizes the 24-GHz transceiver chip from Infineon, with the model number BGT24LTR11N16 [25]. This chip encompasses the essential VCO and mixer required for the FLL.

The signal output from the VCO at frequency ω_0 is described. For the sake of simplifying the mathematical derivation, this study omits the amplitude portion and focuses solely on the phase variation. Hence, the signal can be expressed as

$$V_{TX}(t) = \cos(\omega_0 t). \tag{2}$$

After the signal passes through the power divider, one part is directly input to the mixer as a reference signal. The other part, after being amplified by the amplifier, passes through the sensing device to detect the LUT. The phase shift caused by the LUT ϕ_{LUT}, results in the signal being expressed as

$$V_{RX}(t) = \cos[\omega_0(t - \tau_s) - \phi_{\text{LUT}}]. \tag{3}$$

It is noted that V_{TX} is used as the reference signal, and V_{RX} acts as the sensing signal. Both are fed into a mixer with a sensitivity of k_m, and then passed through the LPF, resulting
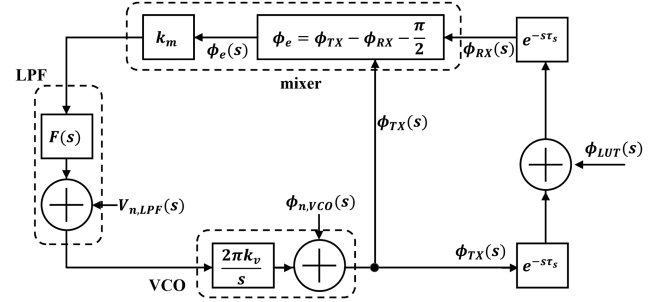

Fig. 7. Frequency analysis diagram of FLL.

in the final output signal

$$V_{\text{LPF}}(t) \approx \frac{1}{2}k_m \cos(\omega_0\tau_s + \phi_{\text{LUT}}). \tag{4}$$

In [26], it is known that the sensing signal $V_{RX}(t)$ and the reference signal $V_{TX}(t)$ are orthogonal due to the action of the loop filter. Therefore, we can substitute $\omega_0\tau_s \approx \frac{\pi}{2}$ into (4)

$$V_{\text{LPF}}(t) \approx -\frac{1}{2}k_m \sin(\phi_{\text{LUT}}). \tag{5}$$

When ϕ_{LUT} is a very small value, (5) can be rewritten as

$$V_{\text{LPF}}(t) \approx -\frac{1}{2}k_m\phi_{\text{LUT}}. \tag{6}$$

It is understood that ϕ_{LUT} and V_{LPF} are linearly related. After V_{LPF} is fed back to the VCO with a sensitivity of k_v, the new output frequency is generated as

$$V'_{\text{LPF}}(t) = \cos\left[\omega_0 t - \int \pi k_m k_v \phi_{\text{LUT}} dt\right]. \tag{7}$$

By simplifying (7), we obtain the phase offset $\Delta\omega_s$ caused by the LUT

$$V'_{\text{LPF}}(t) = \cos\left[(\omega_0 + \Delta\omega_s)t\right]. \tag{8}$$

The aforementioned is the signal analysis of FLL in the time domain. Next, we will analyze it in the frequency domain.

In the previously discussed FLL, the mixer serves as a phase detector. To achieve this, it is essential to maintain orthogonality between the two signals input into the mixer. The frequency analysis diagram for the FLL-based sensor is shown in Fig. 7. In contrast to the works in [24] and [26], where active filters are employed to achieve this, our work utilizes passive filters for realizing the orthogonality effect.

Let us denote ϕ_e as the phase difference between the sensing signal and the reference signal. Considering the reference signal ϕ_{TX} from the VCO, which after undergoing a phase deviation ϕ_{LUT} due to the LUT, results in the received sensing signal ϕ_{RX}, the relationship can be expressed as

$$\phi_e(s) = \phi_{TX}(s) - \phi_{RX}(s) - \frac{\pi}{2} \tag{9}$$

where s denotes the complex frequency. By employing a passive loop filter with a frequency response of F_s, and when the signal delay τ_s caused by the LUT is minimal, (9) can be

reformulated as

$$\phi_e(s) = -\phi_{\text{LUT}}(s)\frac{1-s\tau_s}{1-4\pi k_m k_v \tau_s F(s)} - \frac{\pi}{2}. \quad (10)$$

The frequency response F_s of the passive loop filter is given by

$$F_s = \frac{1+s\tau_p}{1+s(\tau_s+\tau_p)}. \quad (11)$$

When the liquid is injected into the microfluidic channel, and the system reaches a stationary state, by considering t as approaching infinity, we can conclude that

$$\phi_e(t \to \infty) = \lim_{t \to \infty} s\phi_e(s) = 0. \quad (12)$$

When $\phi_e = 0$, substituting into (9) yields:

$$\phi_e = 0 = \phi_{TX}(s) - \phi_{RX}(s) - \frac{\pi}{2} \quad (13)$$

$$\phi_{TX}(s) - \phi_{RX}(s) = \frac{\pi}{2}. \quad (14)$$

When a phase difference of 90° is applied at both ends, it allows the mixer to be used as a phase detector.

The LPF is designed using analog devices' software, ADIS-imPLL. The VCO sensitivity of k_v from the 24-GHz transceiver chip, which originally has a built-in value of 40 MHz/V, is reduced to 20 MHz/V. This adjustment aims to enhance the V_{tune} of the FLL output under the fixed phase shifts cause by the LUT. The transfer function $Z(s)$ for the LPF can be expressed as

$$Z(s) = \frac{V_{\text{out}}}{I_{\text{in}}} = \frac{R2 \cdot C2 \cdot s + 1}{A3 \cdot s^3 + A2 \cdot s^2 + A1 \cdot s} \quad (15)$$

$$A1 = C1 + C2 + C3 \quad (16)$$

$$A2 = (R2 \cdot C2 \cdot C3)$$
$$+ (R2 \cdot C1 \cdot C2)$$
$$+ (R3 \cdot C3 \cdot C1)$$
$$+ (R3 \cdot C3 \cdot C2) \quad (17)$$

$$A3 = C1 \cdot C2 \cdot C3 \cdot R2 \cdot R3. \quad (18)$$

The circuit structure and the simulated $Z(s)$ versus frequency of the LPF are shown in Fig. 8.

C. FLL-Based Sensor

After combining the mentioned FLL, sensing device, and LPF into a complete FLL-based sensor as shown in Fig. 6, the output of the sensor is connected to an Agilent spectrum analyzer N9010 A. Mixtures with EVF ranging from 0% to 100%, with intervals of 10%, are used as the LUT, and the frequency output is observed. The relationship between EVF and output frequency is depicted in the Fig. 9

Given that the FLL-based sensor operates at a frequency of 24 GHz, the output frequency is scaled down by a factor of 16, reducing it to 1.5 GHz. From Fig. 9, under various LUT conditions, the FLL-based sensor can discern and output corresponding frequencies, displaying a linear distribution.
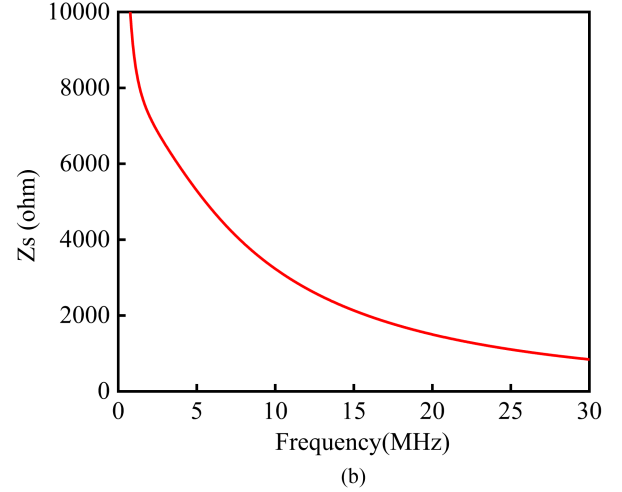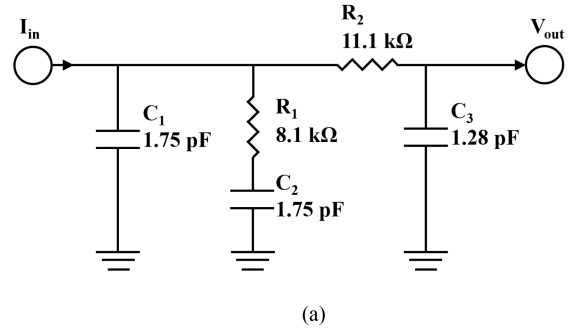

Fig. 8. (a) Circuit structure and (b) $Z(s)$ versus frequency of the LPF.
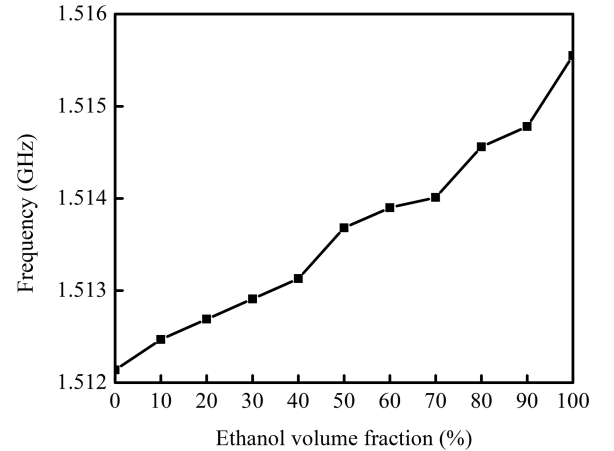
Fig. 9. Concentration versus FLL output frequency for ethanol–water mixture LUT.

III. FREQUENCY DEMODULATOR

Although the proposed sensor is capable of discerning various LUT concentrations, its output consists of frequency-modulated signals. These signals necessitate the use of cumbersome and costly equipment for monitoring. However, by incorporating a frequency demodulator into the sensor's output system, we can convert the frequency into a corresponding voltage, simplifying the observation process.

(a)

(b)

Fig. 10. (a) System block diagram and (b) implementation picture of the frequency demodulator.

Fig. 11. Measured phase difference between two output port of Wilkinson power divider.

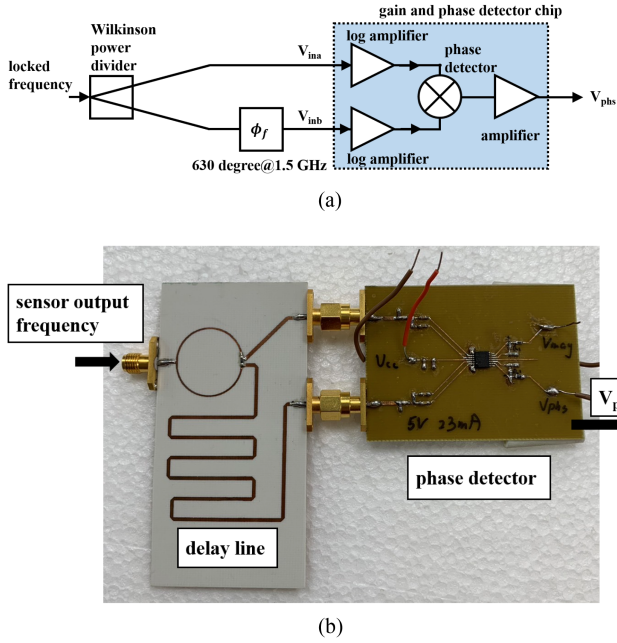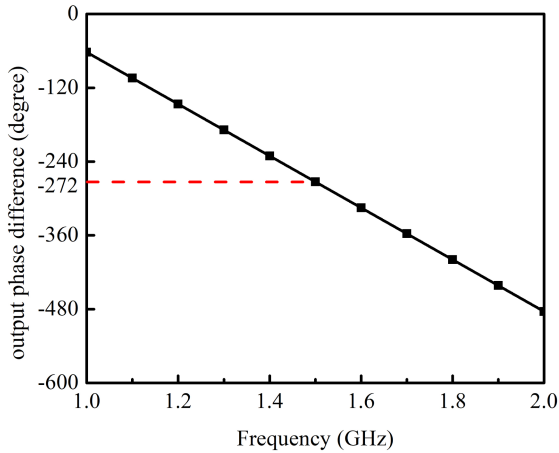As illustrated in Fig. 10(a) and (b), the system block diagram and the implementation of frequency demodulator are shown below. The frequency demodulator comprises a Wilkinson power divider, a transmission line with a 630° phase delay at 1.5 GHz, and is connected with the AD8302 phase detector [27]. By integrating the 630° delay transmission line with the output of the Wilkinson power divider, a physical setup is achieved as depicted in Fig. 10(b). The measured phase difference between the two output ports is presented in Fig. 11. The information obtained from the Fig. 11 indicates that at 1.5 GHz, the output phase difference is 272° plus a full rotation, which is 360°, totaling 632°.

The principle behind this setup is to first split the frequency output from the FLL-based sensor F_{FLL} into two paths using

the power divider. One path $F_{\text{FLL}a}$ is directly fed into the phase detector, while the other path $F_{\text{FLL}b}$ is first routed through the 630° delay transmission line at 1.5 GHz before being input into the phase detector. Equations of $F_{\text{FLL}a}$ and $F_{\text{FLL}b}$ are shown below:

$$F_{\text{FLL}a} = \cos[(\omega_0 + \Delta\omega_s)t] \tag{19}$$

$$F_{\text{FLL}b} = \cos[(\omega_0 + \Delta\omega_s)t + \phi_f] \tag{20}$$

$$V_{\text{phs}} = V_\phi[\phi(F_{\text{FLL}a}) - \phi(F_{\text{FLL}b})] = V_\phi(\phi_f). \tag{21}$$

In this context, $\Delta\omega_s$ represents the phase shift induced by the LUT, whereas ϕ_f denotes the phase delay experienced by the signal as it traverses the transmission line, which exhibits a 630° phase shift at a frequency of 1.5 GHz, and the V_ϕ is the phase slope in mV/°. As mentioned in Fig. 9, FLL-based sensor can generate corresponding frequencies from different EVF of ethanol–water mixtures. When the signal enters the Wilkinson power divider at different frequencies, the phase shifts caused by the 630° phase shift delay transmission line for these different frequencies will also vary.

Upon the introduction of $F_{\text{FLL}a}$ and $F_{\text{FLL}b}$ into the phase detector, the utilization of logarithmic amplifiers at the input stage of the phase detector not only mitigates additional nonlinear distortion of the input signal but also enables the detection of signals with lower intensity. The system linearizes the output in decibels at the output stage. The voltages V_{la} and currents I_{la}, which enter logarithmic amplifiers with slopes V_{slp} and I_{slp}, respectively, are described by the following equations:

$$V_{la} = V_{\text{slp}}\log\left(\frac{F_{\text{FLL}a}}{F_{\text{FLL}b}}\right) \tag{22}$$

$$I_{la} = I_{\text{slp}}\log\left(\frac{F_{\text{FLL}a}}{F_{\text{FLL}b}}\right). \tag{23}$$

In the phase detector, to achieve a result that represents the phase difference, inputs proportional to the phase division are required. By applying (22) and (23), the result of this division can be obtained. Consequently, the formula for the phase detector is as follows and the phase output voltage V_{phs} can be derived.

To validate the functionality of the frequency demodulator, we employ the N5181 A signal generator from Keysight Technologies to simulate an FLL-based sensor and inputted the corresponding output frequencies measured by the FLL-based sensor for different EVF ethanol–water mixtures, as mentioned earlier. The relationship between the voltage output of the frequency demodulator and the input frequency is depicted in Fig. 12, indicating that the frequency demodulator is capable of converting frequencies corresponding to different ethanol–water mixtures EVFs into corresponding voltages, exhibiting a linear distribution.

IV. 24-GHz MICROFLUIDIC CONCENTRATION SENSOR INTEGRATION AND VERIFICATION

The previous sections have meticulously described the composition, operating principles, and measurement validation of the FLL-based sensor and the frequency demodulator. These include components of the 24-GHz transceiver chip, the
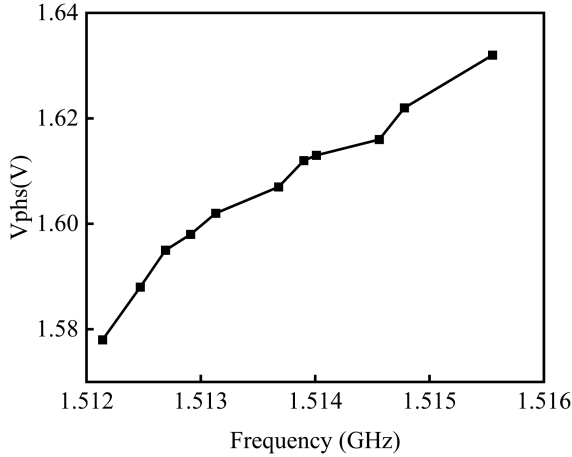
Fig. 12.   Voltage output of the frequency demodulator and the input frequency relationship.
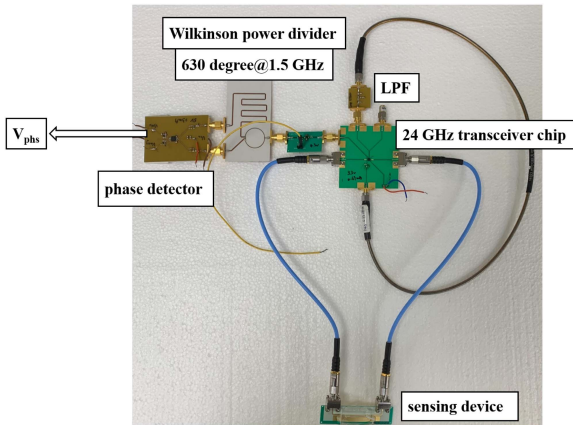

Fig. 13.   Implementation of 24-GHz concentration sensor.

Fig. 14.   Comparison of V_{phs} measured with ethanol–water mixture and after curve fitting.
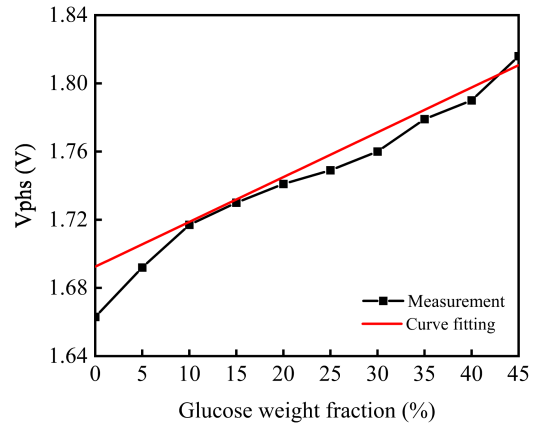
Fig. 15.   Comparison of V_{phs} measured with GWF and after curve fitting.

ACPWR sensing element, the microfluidic channel, and the LPF; as well as the Wilkinson power divider with a 630° phase shift at the output port and the phase detector. This section will detail the assembly of the FLL-based sensor with the frequency demodulator to form a complete 24-GHz FLL-based concentration sensing system. An illustration of the implemented sensor system is provided in Fig. 13, and the system's measurement validation will be conducted using ethanol–water mixtures and glucose–water solutions.

The initial presentation showcases measurements made using an ethanol–water mixture as the LUT for EVF ranging from 0% to 100%, at intervals of 10%, constituting 11 sets of LUT with different concentrations. The relationship between the EVF and the measured output voltage V_{phs} is illustrated in Fig. 14. The results demonstrate a linear distribution. The discrepancy in the initial values between the two experiments could be addressed in future work through calibration of the baseline point.

Following the ethanol–water mixture experiments, the glucose–water solutions were prepared for measurement validation using dry glucose powder GL01250500 from Scharlau, with glucose weight fraction (GWF) concentrations ranging from 0% to 45%, at 5% intervals, resulting in ten groups of test liquids
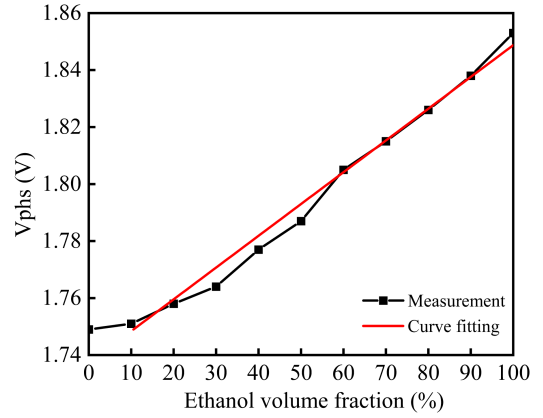
with varying concentrations. The measurement outcomes, as illustrated in the subsequent Fig. 15, demonstrate that, by substituting the LUT with glucose–water solutions, it is possible to output corresponding voltages for different concentrations, thus distinguishing the varying densities of liquids. Moreover, compared with the result after curve fitting, the output voltage displays an approximately linear relationship, which aligns with the initial objectives of the experiment.

Table I presents a comparative analysis of the measurement between dielectric constant sensors and concentration sensors. Notably, in scenarios where a vector network analyzer is not requisite for measurements, the LUT volume required in this study is significantly reduced compared with the work in [14], while simultaneously achieving a markedly enhanced sensitivity. In comparison with the works in [19], [23], and [24], our approach demonstrates a substantially higher sensitivity in terms of frequency percentage change. Meanwhile, relative to the works in [16], [17], [18], [20], and [22], despite similar or smaller LUT volumes in these studies, our EVF sensitivity remains superior. In specific comparison with the work in [22], the LUT employs a glucose–water solution, indicating a narrow range of relative permittivity (ε_r). The performance under

TABLE I
PERFORMANCE COMPARISON OF SENSORS FROM LITERATURE AND THE PROPOSED SENSOR

Ref. No.	Frequency (GHz)	Sensor Technology	ε_r or Concentration Range	LUT Volume (μL)	Requirement of VNA	Sensitivity
[13]	2.3	CSRR-based sensor	EVF 0%–100%	N/A	Yes	0.35 kHz/%
[14]	3.4−3.8	SIW-based sensor	IVF 0%–100%	3500	Yes	4.19 MHz/%
[16]	1.53	Filter-based sensor with gain/phase detector	EVF 10%–90%	8	No	0.48 mV/%
[18]	10.4	PLL-based oscillator	MVF 0%–100%	20	No	0.9437 MHz/%
[23]	3.75−3.862	SIW-based sensor	EVF 0%–100%	101	No	1.1 kHz/%
[24]	5.98	FLL-based sensor	EVF 0%–90%	100	No	98 kHz/%
[28]	1.156	Loss-Compensated SRR	GWF 0%–15.25%	10	Yes	2.75 kHz/%
[29]	4.9	DSRR	GWF 0%–0.6%	10	Yes	200 kHz/%
[22](ethanol)	2	TCLR sensing oscillator	EVF 0%–100%	9	No	0.33 mV/%
This work(ethanol)	24	FLL-based microfluidic sensor	EVF 0%–100%	20	No	1.16 mV/%, 34.1 kHz/%
[22](glucose)	2	TCLR sensing oscillator	GWF 5%–35%	9	No	1.43 mV/%
This work(glucose)	24	FLL-based microfluidic sensor	GWF 0%–45%	20	No	3.4 mV/%

these conditions is comparable. However, the utilization of an FLL-based sensor in our study offers improved environmental emission characteristics.

V. CONCLUSION

This study introduces a 24-GHz microfluidic concentration sensor system composed of an FLL-based sensor and a frequency demodulator. It successfully discriminates between different concentrations of LUT solutions, converting them into corresponding voltages results in a linear distribution when compared with the results from curve fitting. The feasibility of the FLL is validated through mathematical derivations in both the time and frequency domains, and this article provides the mathematical formulae for the frequency demodulator's conversion of frequency shifts into voltages. It also thoroughly details the functionalities of components, such as the sensing element, microfluidic channel, loop filter, 24-GHz transceiver chip, Wilkinson power divider, 630° delay line, and phase detector. Measurement validation is performed using alcohol–water solutions with EVFs from 0% to 100% and glucose–water solutions with glucose weight fractions from 0% to 45%, where each concentration can be clearly distinguished.

When compared with other active sensor systems, this work showcases high sensitivity, low test liquid volume, and compact system size. It detects different LUT concentrations without the need for expensive frequency measurement equipment, such as network analyzers, saving both space and cost. There is potential for further miniaturization and improvement of the sensor system. By integrating the system onto a chip and incorporating IoT technology, it could be adapted for home-based biological sample measurements, such as saliva, urine, or blood.

REFERENCES

[1] A. Kumar, A. Parihar, U. Panda, and D. S. Parihar, "Microfluidics-based point-of-care testing (POCT) devices in dealing with waves of COVID-19 pandemic: The emerging solution," *ACS Appl. Bio Materials*, vol. 5, no. 5, pp. 2046–2068, 2022.

[2] S. Sachdeva, R. W. Davis, and A. K. Saha, "Microfluidic point-of-care testing: Commercial landscape and future directions," *Front. Bioeng. Biotechnol.*, vol. 8, Jan. 2021, Art. no. 602659.

[3] T. Han et al., "Microfluidic paper-based analytical devices in clinical applications," *Chromatographia*, vol. 83, no. 6, pp. 693–701, Jun. 2020.

[4] C. W. Shields, C. D. Reyes, and G. P. López, "Microfluidic cell sorting: A review of the advances in the separation of cells from debulking to rare cell isolation," *Lab Chip*, vol. 15, no. 5, pp. 1230–1249, Mar. 2015.

[5] Z. Li, X. Xu, D. Wang, and X. Jiang, "Recent advancements in nucleic acid detection with microfluidic chip for molecular diagnostics," *TrAC Trends Anal. Chem.*, vol. 158, 2023, Art. no. 116871.

[6] H. Yang and M. A. Gijs, "Micro-optics for microfluidic analytical applications," *Chem. Soc. Rev.*, vol. 47, no. 4, pp. 1391–1458, 2018.

[7] E. Weber and M. J. Vellekoop, "Optofluidic micro-sensors for the determination of liquid concentrations," *Lab Chip*, vol. 12, no. 19, pp. 3754–3759, Oct. 2012.

[8] A. Ebrahimi and K. Ghorbani, "High-sensitivity detection of solid and liquid dielectrics using a branch line coupler sensor," *IEEE Trans. Microw. Theory Techn.*, vol. 71, no. 12, pp. 5233–5245, Dec. 2023.

[9] J. Muñoz-Enano, P. Vélez, P. Casacuberta, L. Su, and F. Martín, "Reflective-mode phase-variation permittivity sensor based on a step-impedance microstrip line terminated with a slot resonator for solid and liquid characterization," *IEEE Trans. Microw. Theory Techn.*, vol. 72, no. 4, pp. 2519–2533, Apr. 2024.

[10] A. Ebrahimi, J. Scott, and K. Ghorbani, "Ultrahigh-sensitivity microwave sensor for microfluidic complex permittivity measurement," *IEEE Trans. Microw. Theory Techn.*, vol. 67, no. 10, pp. 4269–4277, Oct. 2019.

[11] A. A. Abduljabar, D. J. Rowe, A. Porch, and D. A. Barrow, "Novel microwave microfluidic sensor using a microstrip split-ring resonator," *IEEE Trans. Microw. Theory Techn.*, vol. 62, no. 3, pp. 679–688, Mar. 2014.

[12] A. A. Abduljabar, A. Porch, and D. A. Barrow, "Real-time measurements of size, speed, and dielectric property of liquid segments using a microwave microfluidic sensor," in *Proc. IEEE MTT-S Int. Microw. Symp.*, 2014, pp. 1–4.

[13] E. L. Chuma, Y. Iano, G. Fontgalland, and L. L. Bravo Roger, "Microwave sensor for liquid dielectric characterization based on metamaterial complementary split ring resonator," *IEEE Sensors J.*, vol. 18, no. 24, pp. 9978–9983, Dec. 2018.

[14] G. M. Rocco et al., "3-D printed microfluidic sensor in SIW technology for liquids' characterization," *IEEE Trans. Microw. Theory Techn.*, vol. 68, no. 3, pp. 1175–1184, Mar. 2020.

[15] A. Hamid Allah, G. A. Eyebe, and F. Domingue, "Fully 3D-printed microfluidic sensor using substrate integrated waveguide technology for liquid permittivity characterization," *IEEE Sensors J.*, vol. 22, no. 11, pp. 10541–10550, Jun. 2022.

[16] T.-K. Nguyen and C.-H. Tseng, "New radio-frequency liquid permittivity measurement system using filter-based microfluidic sensor," *IEEE Sensors J.*, vol. 23, no. 12, pp. 12785–12795, Jun. 2023.

[17] A. A. Helmy et al., "A self-sustained CMOS microwave chemical sensor using a frequency synthesizer," *IEEE J. Solid-State Circuits*, vol. 47, no. 10, pp. 2467–2483, Oct. 2012.

[18] O. Elhadidy, M. Elkholy, A. A. Helmy, S. Palermo, and K. Entesari, "A CMOS fractional- n PLL-based microwave chemical sensor with 1.5% permittivity accuracy," *IEEE Trans. Microw. Theory Techn.*, vol. 61, no. 9, pp. 3402–3416, Sep. 2013.

[19] A. A. Helmy and K. Entesari, "A 1-8 GHz miniaturized spectroscopy system for permittivity detection and mixture characterization of organic chemicals," *IEEE Trans. Microw. Theory Techn.*, vol. 60, no. 12, pp. 4157–4170, Dec. 2012.

[20] C.-H. Pai and C.-H. Tseng, "A new microwave oscillator-based microfluidic sensor for complex permittivity measurement," in *Proc. IEEE/MTT-S Int. Microw. Symp.*, 2023, pp. 967–970.

[21] V. Sekar, W. J. Torke, S. Palermo, and K. Entesari, "A novel approach for dielectric constant measurement using microwave oscillators," in *Proc. IEEE MTT-S Int. Microw. Symp.*, 2011, pp. 1–4.

[22] C.-H. Tseng, C.-H. Pai, and H.-C. Chang, "A new microwave oscillator-based microfluidic dielectric sensor," *IEEE Trans. Microw. Theory Techn.*, vol. 72, no. 1, pp. 628–637, Jan. 2024.

[23] A. A. Helmy, S. Kabiri, M. M. Bajestan, and K. Entesari, "Complex permittivity detection of organic chemicals and mixtures using a 0.5–3 GHz miniaturized spectroscopy system," *IEEE Trans. Microw. Theory Techn.*, vol. 61, no. 12, pp. 4646–4659, Dec. 2013.

[24] C.-H. Tseng and C.-Y. Yang, "Novel microwave frequency-locked-loop-based sensor for complex permittivity measurement of liquid solutions," *IEEE Trans. Microw. Theory Techn.*, vol. 70, no. 10, pp. 4556–4565, Oct. 2022.

[25] Infineon Technologies AG, BGT24LTR11n16 Radar Sensor Data Sheet, 2018. [Online]. Available: https://www.infineon.com/cms/en/product/sensor/radar-sensors/radar-sensors-for-iot/24ghz-radar/bgt24ltr11n16/

[26] K.-C. Peng, M.-C. Sung, F.-K. Wang, and T.-S. Horng, "A wireless-frequency-locked-loop-based vital sign sensor with quadrature tracking and phase-noise reduction capability," *IEEE Sensors J.*, vol. 21, no. 8, pp. 9706–9715, Apr. 2021.

[27] Analog Devices, AD8302: LF-2.7 GHz RF/IF Gain and Phase Detector Data Sheet, 2018. [Online]. Available: https://www.analog.com/media/en/technical-documentation/data-sheets/ad8302.pdf

[28] M. Abdolrazzaghi, N. Katchinskiy, A. Y. Elezzabi, P. E. Light, and M. Daneshmand, "Noninvasive glucose sensing in aqueous solutions using an active split-ring resonator," *IEEE Sensors J.*, vol. 21, no. 17, pp. 18742–18755, Sep. 2021.

[29] M. Abdolrazzaghi and M. Daneshmand, "Exploiting sensitivity enhancement in micro-wave planar sensors using intermodulation products with phase noise analysis," *IEEE Trans. Circuits Syst. I: Reg. Papers*, vol. 67, no. 12, pp. 4382–4395, Dec. 2020.

Hsiu-Che Chang was born in Chiayi, Taiwan, in 1999. He received the B.S. degree in international program in electrical and communication engineering from YuanZe University, Taoyuan, Taiwan, in 2021, and the M.S. degree in electronic and computer engineering from the National Taiwan University of Science and Technology, Taipei, Taiwan, in 2023. He is currently working toward the Ph.D. degree in communication engineering with National Taiwan University, Taipei.

His current research focuses on RF circuit design.

Chung-Tse Michael Wu (Senior Member, IEEE) received the B.S. degree in electrical engineering from National Taiwan University (NTU), Taipei, Taiwan, in 2006, and the M.S. and Ph.D. degrees in electrical engineering from the University of California at Los Angeles (UCLA), Los Angeles, CA, USA, in 2009 and 2014, respectively.

From 2008 to 2014, he was a Graduate Student Researcher with the Microwave Electronics Laboratory, UCLA. In 2009, he was a Summer Intern with Bell Labs, Murray Hill, NJ, USA. In 2012, he was a Special-Joint Researcher with Japan Aerospace Exploration Agency, Sagamihara, Japan. From 2014 to 2017, he was an Assistant Professor with the Department of Electrical and Computer Engineering, Wayne State University (WSU), Detroit, MI, USA. In 2017, he joined Rutgers University, New Brunswick, NJ, USA, as an Assistant Professor and was promoted to tenured Associate Professor in 2022. Since 2024, he has been an Associate Professor with NTU. His research interests include applied electromagnetics, antennas, passive/active microwave and millimeter-wave components, RF systems, and metamaterials.

Dr. Wu is currently an Associate Editor for IEEE MICROWAVE AND WIRELESS TECHNOLOGY LETTERS, IEEE JOURNAL OF ELECTROMAGNETICS, RF AND MICROWAVES IN MEDICINE AND BIOLOGY, and IEEE ACCESS. In addition, he is a Member of the Technical Committee for IEEE MTT-28 and MTT-4 and holds the position of Vice Chair for the Joint AP/ED/MTT Chapter of IEEE Princeton Central Jersey Section. He was the recipient of the National Science Foundation Faculty Early Career Development Award, WSU College of Engineering Faculty Research Excellence Award in 2016, Defense Advanced Research Projects Agency (DARPA) Young Faculty Award in 2019, DARPA Director's Fellowship Award in 2021, and in 2022, the Board of Trustees Research Fellowship for Scholarly Excellence with Rutgers University.

Chao-Hsiung Tseng (Senior Member, IEEE) received the Ph.D. degree in communication engineering from National Taiwan University, Taipei, Taiwan, in 2004.

From 2004 to 2005, he was a Postdoctoral Research Fellow with the Department of Electrical Engineering, National Taiwan University. From 2005 to 2006, he was with the Department of Electrical Engineering, University of California at Los Angeles, Los Angeles, CA, USA, as a Visiting Scholar. In 2006, he joined the faculty of the Department of Electronic and Computer Engineering, National Taiwan University of Science and Technology, Taipei, where he became a full Professor in 2013 and a Distinguished Professor in 2021. He was the Vice Chairperson of the Department of Electronic and Computer Engineering from 2011 to 2012, and Chairperson of the Inter-disciplinary Bachelor's Program from 2012 to 2013. From 2013 to 2014, he was with the Department of Electrical and Computer Engineering, University of Florida, Gainesville, FL, USA, as a Visiting Scholar. In 2024, he joined Yang Ming Chiao Tung University, Hsinchu, Taiwan, as a Professor of the Institute of Space Systems Engineering. His research interests include microwave communication electronics, radio-frequency microfluidic sensors, noncontact vital-sign radar sensors, and microwave circuits and modules.

Dr. Tseng is currently a Member of IEEE MTT-S Technical Committees (TC-28 Biological Effects and Medical Applications). He was the recipient of 2008, 2014, 2018, and 2022 Teaching Awards and the 2012, 2020, and 2021 Research Awards from the National Taiwan University of Science and Technology.